Inorganic Chemistry

pubs.acs.org/IC Article

{040/110} Facet Isotype Heterojunctions with Monoclinic Scheelite $BiVO_4$

Basudev Baral and Kulamani Parida*

Cite This: *Inorg. Chem.* 2020, 59, 10328−10342 Read Online

ACCESS | Metrics & More | Article Recommendations

ABSTRACT: Controlling the phase, crystallinity, and microstructure and fabricating a facet isotype heterojunction with a proscribed reduction−oxidation facet exposure factor have a strong constructive effect toward photoexciton separation and migration. In this respect, here diverse synthetic courses such as calcination ($BiVO_4$-C), hydrothermal treatment ($BiVO_4$-H), and a reflux method ($BiVO_4$-R) are introduced to fabricate various hierarchical morphologies of highly crystalline monoclinic scheelite bismuth vanadate ($BiVO_4$) with different redox facet exposure factors that have been well established by X-ray diffraction, Fourier transform infrared spectroscopy, field emission scanning electron microscopy, and transmission electron microscopy analysis. The analytical and experimental investigations revealed superior photocatalytic upshots of a $BiVO_4$-R {040/110} facet isotype heterojunction toward levofloxacin (LVF) detoxification (71.2%, 120 min) and the water oxidation reaction (530.6 μmol, 120 min) relative to $BiVO_4$-C (42.3%, 434.2 μmol) and $BiVO_4$-H (60.4%, 494.8 μmol). Accordingly, the $BiVO_4$-R {040/110} facet isotype heterojunction (145.6 $\mu A/cm^2$) expressed an enhanced photocurrent in comparison to pristine $BiVO_4$-C (75.5 $\mu A/cm^2$) and $BiVO_4$-H (113.1 $\mu A/cm^2$). The superior photocatalytic redox efficiency was attributed to well-exposed {040} reduction and {110} oxidation facets and a superior relative {040} facet exposure factor provoking an enhanced charge carrier separation over a $BiVO_4$-R {040/110} facet isotype heterojunction. The spatial exciton separation over the $BiVO_4$-R sample was well established by numerous analytical and experimental investigations. The effectual associations among physicochemical, photoelectrochemical properties, {040/110} facet isotype heterojunction, relative reduction−oxidation facet exposure factor, and photocatalytic performances of fabricated $BiVO_4$ microstructures were well established, and the upshots of this research were discussed finely. The research signifies an effectual direction for morphology and relative reduction−oxidation facet exposure factor controlled fabrication of facet isotype heterojunction based materials for superior photocatalysis and could be advantageous for supplementary research areas.

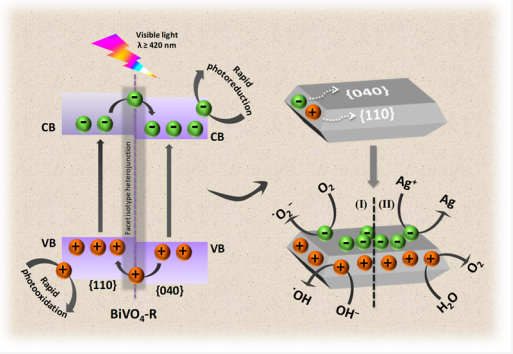

1. INTRODUCTION

Challenging the current dilemma of energy-environmental cataclysm, redox course driven semiconductor-based photocatalysis has emerged as an eco-efficient and sustainable resolution.[1,2] Despite the enormous progress that has been made, surface incompatibility provoked rapid exciton recombination suppresses the expected redox efficiency of traditional heterojunction materials. Moreover, to triumph over the inefficiencies of traditional heterojunctions, n−n isotype heterojunctions between materials with the same charge carrier such as $ZnWO_4/Bi_2WO_6$, $BiPO_4/Bi_2WO_6$, g-C_3N_4/TiO_2, and $Bi_{3.64}Mo_{0.36}O_{6.55}/Bi_2MoO_6$, etc. and crystal phase isotype heterojunctions between different crystal phases of a pristine material such as α-Ga_2O_3/β-Ga_2O_3, CN-T/CN-U, GCN/CCN, and TiO_2(A)/TiO_2(R) have also been introduced.[3−10] Captivatingly, an $InS_3/BiVO_4$ n−n isotype and an M-$BiVO_4$/T-$BiVO_4$ crystal phase isotype heterojunction toward antibiotic detoxification and water oxidation were successfully reported by our group.[11,12] Superior interfacial compatibilities and a space charge accumulation/depletion region promoted exciton separation over these heterojunction heighten the photo redox efficiency. Nevertheless, to broaden the research further, a facet isotype heterojunction was introduced over different exposed reduction−oxidation facets of pristine semiconducting materials. Various widely reported materials with crystal facet engineering include TiO_2, BiOCl, $BiVO_4$, $NaTaO_3$, $ZnFe_2O_4$, CdS, $BiOIO_3$, etc.[13−22] The thermodynamic separation of excitons over the active facets facilitates the overall redox process.

Received: May 19, 2020
Published: June 25, 2020

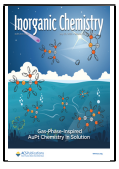

https://dx.doi.org/10.1021/acs.inorgchem.0c01465
Inorg. Chem. 2020, 59, 10328−10342

From this perspective, the monoclinic scheelite $BiVO_4$ has evolved as an appealing metal oxide photocatalytic material for a crystal facet engineered isotype heterojunction, as its efficiency has been reported to be greatly exaggerated by alteration of the microstructure.[16,17,23−28] The controlled exposure of oxidation {110} and reduction facets {040} of monoclinic scheelite $BiVO_4$ adds constructive effects toward exciton separation over the respective energy band edges of an inbuilt facet isotype heterojunction.[16−18,27−31] Moreover, a narrow band gap of 2.3−2.4 eV, superior photostability, nontoxicity, and superior $Bi_{6s}-O_{2p}$ hybrid orbital aggravated visible light absorption ability are the reasonable key factors making the monoclinic scheelite $BiVO_4$ a desirable alternative to conventional UV-active titania (TiO_2) and tetragonal scheelite/zircon phase $BiVO_4$ based photocatalysts in the progressive research field.[1,2,11] Furthermore, Bi−O bond distortion provoked enhanced exciton separation and the destructive effect of $[VO_4]$ tetrahedron provoked superior water oxidation tendency of the monoclinic scheelite $BiVO_4$ attest to its novelty.[11,23]

Nevertheless, research exposing the effective involvement of physicochemical features, electrochemical properties, {040/110} crystal facet isotype heterojunctions, and the relative exposure factors of reduction−oxidation facets of $BiVO_4$ toward superior photocatalytic levofloxacin detoxification and water oxidation has been unavailable so far. Accounting for the above scenario herein, we fabricated various hierarchical morphologies of highly crystalline monoclinic scheelite $BiVO_4$ with varying redox facet exposure factors via diverse synthetic routes such as calcination ($BiVO_4$-C), hydrothermal treatment ($BiVO_4$-H), and a reflux method ($BiVO_4$-R) and investigated the efficiencies of the fabricated microstructure toward levofloxacin detoxification and the water oxidation reaction. The crystallographic features contributing toward redox efficiency have been well determined by X-ray diffraction (XRD) analysis. The photophysical properties were well established by a UV−visible diffuse reflectance spectroscopy (UV−vis DRS) analysis. A Mott−Schottky (MS) analysis was executed to investigate the charge carrier characteristics of fabricated samples. The nature of the exciton separation over the photocatalysts was well exposed by photoluminescence (PL), electrochemical impedance spectroscopy (EIS), carrier density, linear sweep voltammetry (LSV), and Bode analysis. The microstructures, surface morphologies, existence of {040/110} facet isotype heterojunctions, and relative facet exposure factors of the fabricated samples were well observed by field emission scanning electron microscopy (FESEM) analysis. Transmission electron microscopy (TEM) and high-resolution transmission electron microscopy (HRTEM) analyses were carried out to validate the {040/110} facet isotype heterojunction provoked exciton separation process. A comparative investigation on the effective association among physicochemical and electrochemical properties, {040/110} crystal facet isotype heterojunctions, and relative exposure factors of oxidation−reduction facets toward the superior photocatalytic redox efficiency of $BiVO_4$ was neatly ascertained and discussed.

2. EXPERIMENTAL SECTION

2.1. Chemicals and Reagents. Analytical grades of bismuth nitrate pentahydrate ($Bi(NO_3)_3{\cdot}5H_2O$, 99%), ammonium metavanadate (NH_4VO_3, 99%), urea ($CO(NH_2)_2$, 99%), ammonium hydroxide (NH_4OH, 28−30%), nitric acid (HNO_3, 69%), and silver nitrate ($AgNO_3$, 99%) from Merck were used without any additional refinement for material fabrication. Double-distilled deionized water (DI-H_2O) was used throughout the experiments. Analytical grade ethanol (C_2H_5OH, 99.9%) was used for washing.

2.2. Fabrication of Hierarchical Microstructures of $BiVO_4$. About 20 mmol of $Bi(NO_3)_3{\cdot}5H_2O$ and 20 mmolof NH_4VO_3 were added to each of three distinct beakers containing 165 mL of 2 M dilute HNO_3 (SOL-A), 160 mL of 2 M dilute HNO_3 (SOL-B), and 106 mL of 1 M dilute HNO_3 (SOL-C). The SOL-A was stirred for 2 h magnetically until a homogeneous yellow solution was obtained followed by slow addition of NH_4OH until pH 9. The precipitate that formed was washed (H_2O, C_2H_5OH) and dried in a hot air oven (70 °C, 24 h). The product was then finely ground followed by calcination at 500 °C for 5 h (10 °C/min). The sample was collected and assigned the name $BiVO_4$-C. The pH of SOL-B was adjusted to 2. The suspension that formed was then aged (2 h) followed by hydrothermal treatment of the bottom yellow precipitate (200 °C, 24 h). The product that formed was washed (H_2O, C_2H_5OH), dried in a hot air oven (70 °C, 24 h), and assigned the name $BiVO_4$-H. SOL-C was stirred followed by slow addition of 10 g of $CO(NH_2)_2$. The suspension was refluxed (84 °C, 24 h). The precipitate that formed was then washed (H_2O, C_2H_5OH), dried in a hot air oven (70 °C, 24 h), and assigned the name $BiVO_4$-R. All of the fabricated samples were collected and ground well for further characterizations (Scheme 1).[11,27,32,33]

Scheme 1. Illustration of Diverse Fabrication Techniques for Hierarchical Microstructures of Monoclinic Scheelite $BiVO_4$ Samples

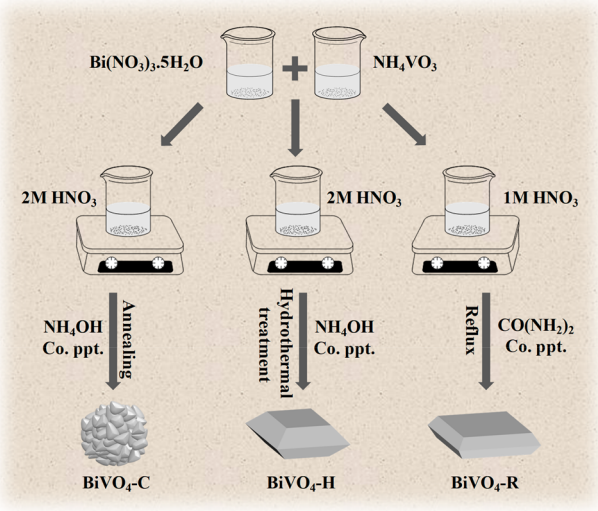

2.3. Fabrication of Ag-$BiVO_4$-R. The successful deposition of Ag nanoparticles over the $BiVO_4$-R sample was carried out via a photodeposition technique. In brief, 300 mg of the $BiVO_4$-R sample was well dispersed in 35 mL of a DI-H_2O/methanol mixture (4/1) via ultrasonication for 30 min. Subsequently, 3.3 mL of an $AgNO_3$ aqueous solution (10 g L^{-1}) was added dropwise to the above suspension with stirring for 30 min followed by visible-light irradiation for 2 h by a 300 W Xe lamp. The resulting suspension was then collected, washed (DI-H_2O, ethanol), dried in a hot air oven (60 °C for 12 h), and assigned the name Ag-$BiVO_4$-R. The fabricated yellowish green Ag-$BiVO_4$-R sample was collected and ground well for further characterizations.[27,29]

2.4. Analytical Characterizations. Crystallographic features were cautiously examined in a Rigaku Ultima IV X-ray diffractometer (Cu Kα, λ = 1.5 Å, 2θ = 10−80°, 5° min^{-1}, 40 kV, 40 mA). A Zeiss Supra 55 field emission scanning electron microscope was employed to examine the microstructure and surface morphological information. Photophysical investigations were retrieved from a JASCO 750 UV−

https://dx.doi.org/10.1021/acs.inorgchem.0c01465
Inorg. Chem. 2020, 59, 10328−10342

visible diffuse reflectance spectrometer ($BaSO_4$ reference). Photoluminescence spectra were precisely examined by deploying a JASCO FP8300 spectrofluorometer (λ_{ex} = 325 nm). A JASCO FT/IR-4600 Fourier transform infrared spectrometer was utilized to neatly analyze the bond vibrational chemistry (KBr matrix). Transmission electron microscopy and high-resolution transmission electron microscopy was carried out to study the surface morphology, deploying a Philips Tecnai G2 instrument (200 kV). The surface chemical characteristics of fabricated materials were investigated by a VG Microtech Multilab ESCA 3000 XPS instrument (Al Kα, 1486.7 eV, C 1s 284.9 eV).

2.5. Electrochemical Measurements. An IVIUM n STAT electrochemical workstation with a conventional three-electrode Pyrex electrochemical cell (working electrode Pt, Ag/AgCl, 0.1 M Na_2SO_4, pH 6.1) was employed to examine photoelectrochemical data. Working electrodes were fabricated by an electrophoretic deposition method in a 20 mL acetone dispersion of 20 mg of the photocatalyst and 20 mg of iodine. The coating surface areas of FTOs (fluorine-doped tin oxide) were maintained to 1 cm × 1 cm under a controlled potentiostatic bias (60 V, 5 min). Linear sweep voltammetry (LSV, −1 to +1 V) analysis, electrochemical impedance spectroscopy (EIS, 0.1−10000 Hz, 0.63 V amplitude, 0 bias), and Bode measurements were executed under visible-light irradiation (300 W xenon, cut off filter ≥400 nm). The Mott−Schottky analysis was carried out in the dark (500 Hz, 25 mV). No photoresponse was observed for FTO without a catalyst coating. The photocurrent steadiness was measured by chronoamperometric (CA) analysis (600 s, 0.6 V). Transient photocurrent measurements were carried out under chopped visible-light illumination (300 s, 0.6 V).

2.6. Photocatalytic Levofloxacin Detoxification. A quartz reactor was employed to examine photocatalytic levofloxacin detoxification under irradiation of visible light (300 W Xe lamp, $\lambda \geq 420$ nm, 100 mW/cm^2). Before photoirradiation, a suspension of 20 mg of the catalyst in 20 mL of a levofloxacin aqueous solution with 20 mg L^{-1} concentration was stirred magnetically in the dark for 30 min to enable an adsorption−desorption equilibrium. The resulting suspension was centrifuged and analyzed in a UV−vis spectrometer at 288 nm.[34−36] The process was repeated at varying reaction times to evaluate the rate and the reaction kinetics.

2.7. Photocatalytic Water Oxidation Reaction. A sealed quartz batch reactor (100 mL capacity) with a temperature controller was employed to examine the water oxidation reaction under visible light irradiation (300 W Xe lamp, $\lambda \geq 420$ nm). First a suspension of 20 mg of the catalyst in 20 mL of a 0.05 M $AgNO_3$ aqueous solution was purged with nitrogen for 30 min preirradiation at room temperature. The source was maintained 10 cm away from the suspension. A molecular sieve (5 Å) column GC-17A gas chromatography instrument with a thermal conductivity detector (TCD) was employed to characterize evolved O_2.

3. RESULTS AND DISCUSSION

FESEM and HRTEM analyses were carried out to better investigate the microstructure and surface morphology of the fabricated samples (Figure 1). As shown in Figure 1a, the pristine $BiVO_4$-C appears to have a dense microspherical structure composed of irregular-polyhedral crystals.[11,23] The minuscule pores near the junction of nanopolyhedral structures in the microstructures are ascribed to gas amputation during the calcination process. The irregular Anonna reticulate shaped microstructures have an average particle size of 3.4−9.6 μm. The resultant TEM image of the fabricated $BiVO_4$-C sample exhibits a microspherical morphology with a well-defined outline, which is in good agreement with the FESEM results (Figure 1b). Furthermore, a high-resolution FESEM image of $BiVO_4$-H (Figure 1c) shows a truncated-bipyramidal morphology with a smooth surface and two {040}, four {110}, and four {011} well-exposed facets.[27−29,33] The average particle size of $BiVO_4$-H was evaluated to be 1.5−4 μm. The respective TEM

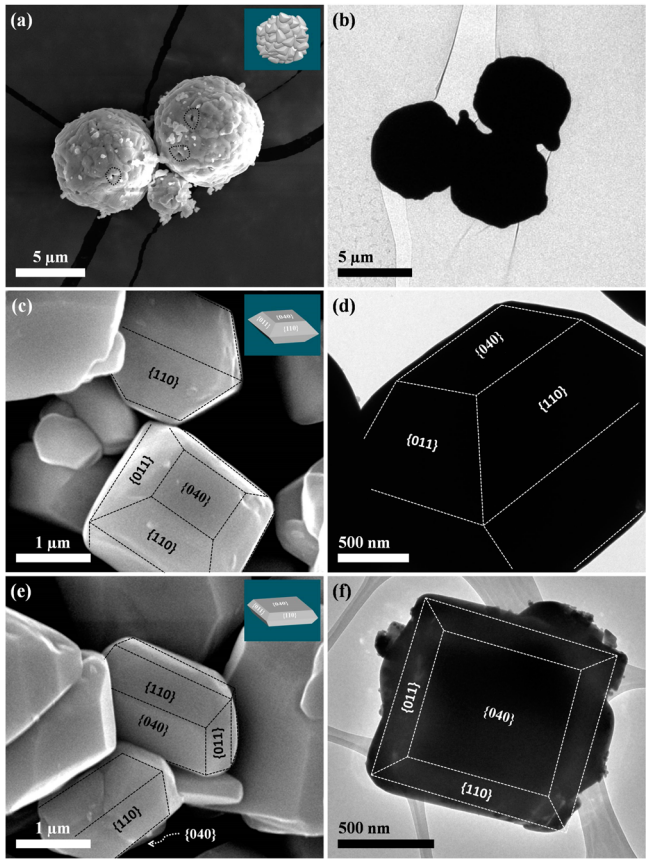

Figure 1. Respective FESEM and TEM images of fabricated monoclinic scheelite (a, b) $BiVO_4$-C, (c, d) $BiVO_4$-H, and (e, f) $BiVO_4$-R samples.

image of the $BiVO_4$-H sample (Figure 1d) illustrates a truncated-bipyramidal morphology with well-defined outlines analogous to the respective FESEM images. Figure 1e represents the FESEM image of the $BiVO_4$-R sample. Microparticles with a truncated-bipyramidal shape with two {040}, four {110}, and four {011} highly exposed facets are well observed.[27−29,33] The approximate average particle size was calculated to be 1.5−5 μm. Expectedly, an analogous truncated-bipyramidal morphology with well-defined outlines was also observed for the $BiVO_4$-R sample (Figure 1f).

The exposure of various {040}, {110}, and {011} facets affecs the exciton separation ability and thus affects the overall redox efficiency of the photocatalysts. The {040} facet is composed of a BiV_4 multiatomic center, while the {110} and {011} facets are composed of Bi_4V_2, thus suggesting analogous characteristics of {110} and {011} exposed facets.[33] The drift velocity of photoexcited electrons over the {040} facet was reported to be greater than that of the {110} facet due to the lower effective mass of electrons.[27,28,30,37,38] Moreover, the densities of states near the valence band maximum (VB_{max}) and conduction band minimum (CB_{min}) of {011} is more localized in comparison to those for the {040} facet.[27,28,30,38] Furthermore, lower band edge potentials of the {040} facet in comparison to the {110} facet favors thermodynamic exciton separations over the exposed facets of inbuilt {040/110} facet isotype heterojunctions.[29,33,38] Consequently, photoexcited electrons tend to move over {040} reduction facets while causing the accumulation of photogenerated holes over {110} oxidation facets, thus promoting the development of built-in

https://dx.doi.org/10.1021/acs.inorgchem.0c01465
Inorg. Chem. 2020, 59, 10328−10342

{040/110} facet isotype heterojunctions over $BiVO_4$-H and $BiVO_4$-R samples.[29,30,32,33,37]

In addition, the relative {040} facet exposure percentage of fabricated materials were well-evaluated via a slab-equilibrium model analysis (Scheme 2) to better validate the effective involvement of the exposure ratio toward enhanced activity.[39−41] As illustrated in Figure 1, the $BiVO_4$-C microstructures show no obvious high exposure of {040}, {110}, and {011} active functional facets. However, $BiVO_4$-H and $BiVO_4$-R exhibit well-exposed {040} facets with an average exposure values of 14% and 36%, respectively, thus validating a higher exposure factor of the {040} facet ({040}/{110}) in $BiVO_4$-R in comparison to $BiVO_4$-C and $BiVO_4$-H. This is further explored in the discussion below.

Scheme 2. Schematic Illustration of the Slab-Equilibrium Model of a Monoclinic Scheelite $BiVO_4$ Single Crystal

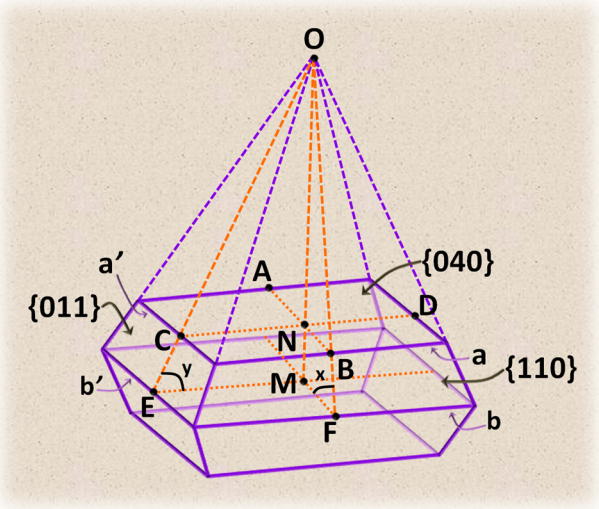

The theoretical assessment of {040} facet exposure percentage was carried out by employing the equations[39−41]

$$A_{\{040\}} = 2aa' \tag{1}$$

$$A_{\{110\}} = 4\left(\frac{1}{2}\mathrm{OF} \times b - \frac{1}{2}\mathrm{OB} \times a\right) \tag{2}$$

$$A_{\{011\}} = 4\left(\frac{1}{2}\mathrm{OE} \times b' - \frac{1}{2}\mathrm{OC} \times a'\right) \tag{3}$$

$$A_{\{040\}}\ (\%) = \frac{A_{\{040\}}}{A_{\{040\}} + A_{\{110\}} + A_{\{011\}}} \times 100 \tag{4}$$

$$A_{\{040\}}\ (\%) = \frac{2aa'}{\left\{2aa' + 4\left(\frac{1}{2}OF \times b - \frac{1}{2}OB \times a\right) + 4\left(\frac{1}{2}OE \times b' - \frac{1}{2}OC \times a'\right)\right\}} \times 100 \tag{5}$$

$$A_{\{040\}}\ (\%) = \frac{2aa'}{\left\{2aa' + 4\left(\frac{1}{2}\frac{\frac{1}{2}b'}{\cos x}b - \frac{1}{2}\frac{\frac{1}{2}a'}{\cos x}a\right) + 4\left(\frac{1}{2}\frac{\frac{1}{2}b}{\cos y}b' - \frac{1}{2}\frac{\frac{1}{2}a}{\cos y}a'\right)\right\}} \times 100 \tag{6}$$

$$A_{\{040\}}\ (\%) = \frac{aa'}{\left\{aa' + \frac{1}{2}(bb' - aa')\left(\frac{1}{\cos x} + \frac{1}{\cos y}\right)\right\}} \times 100 \tag{7}$$

Here, $A_{\{040\}}$, $A_{\{110\}}$, and $A_{\{011\}}$ denote the exposure areas of {040}, {110}, and {011} functional facets of the $BiVO_4$ {040/110}facet isotype heterojunction, respectively. a and a' signify the length and width of the well-exposed {040} facet,

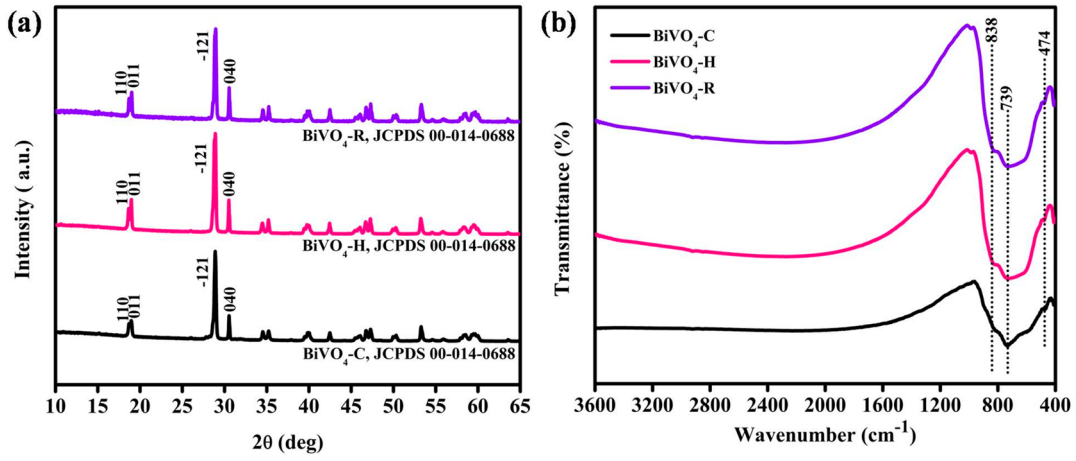

Figure 2. Comparative (a) X-ray diffraction patterns and (b) FT-IR spectra of fabricated monoclinic scheelite $BiVO_4$ samples.

https://dx.doi.org/10.1021/acs.inorgchem.0c01465
Inorg. Chem. 2020, 59, 10328−10342

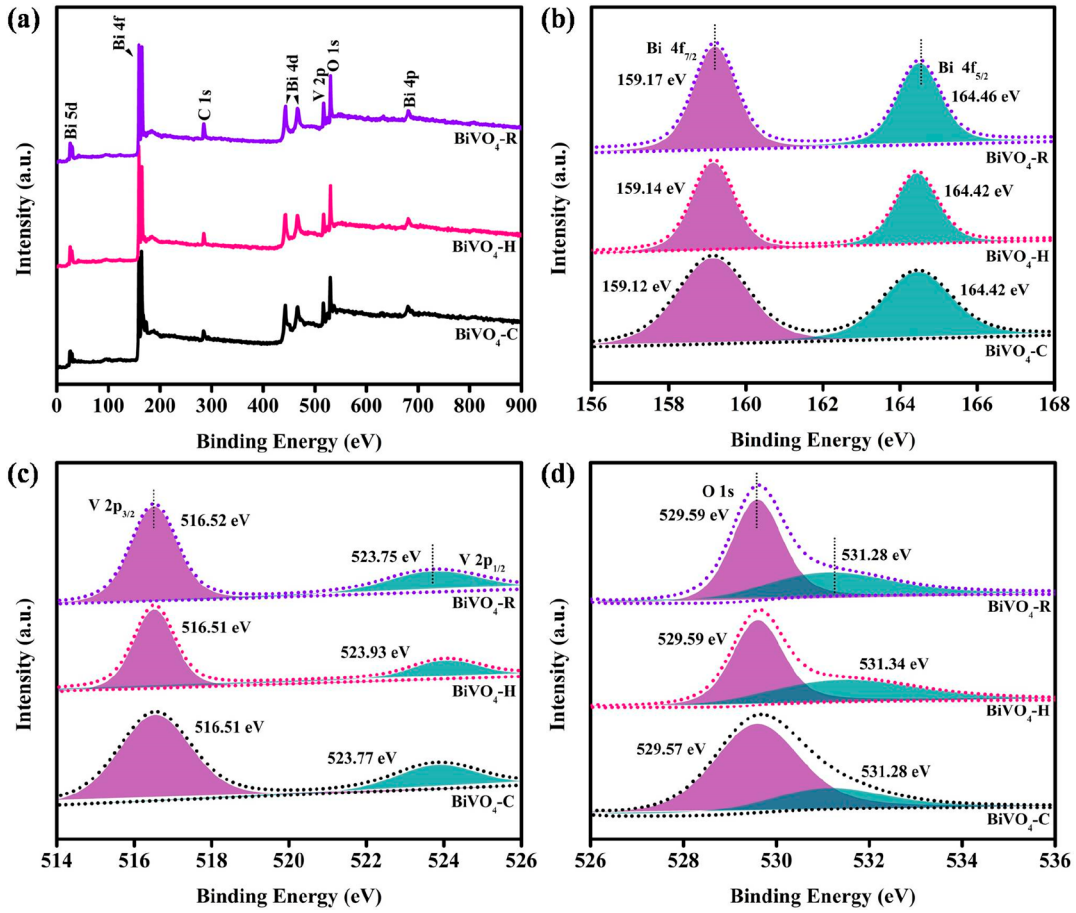

Figure 3. Comparative XPS analysis overview: (a) survey spectrum and (b) Bi 4f, (c) V 2p, and (d) O 1s narrow scan spectra of fabricated monoclinic scheelite $BiVO_4$ samples.

respectively. b and b' signify the length and width of the truncated bipyramid, respectively. x (~66.06°) and y (~66.48°) are the theoretical inclinations of {110} and {011} facets to the {040} facet, respectively.

Powder XRD analysis providing particulars of crystallographic features of the as-synthesized catalysts are shown in Figure 2a. The elemental diffraction peaks of the pristine $BiVO_4$-C, $BiVO_4$-H, and $BiVO_4$-R are well indexed with a body-centered monoclinic scheelite phase of $BiVO_4$ with JCPDS Card No. 00-014-0688.[11,27−29,32,33] The obtained diffraction spectra were devoid of any ancillary impurity peaks, suggesting high purity of the catalysts. Furthermore, the decidedly crystalline characteristics of the pristine synthesized samples were well established by the sharp and intense diffraction signals.

Moreover, the crystallite sizes of the as-synthesized pristine materials were estimated to be 38.88, 64.59, and 64.09 nm for $BiVO_4$-C {112}, $BiVO_4$-H {−121} and $BiVO_4$-R {−121}, respectively, by employing the Scherrer equation (eq 8):[11,26]

$$\text{crystallite size } (D) = k\lambda/\beta \cos\theta \tag{8}$$

Here, λ, β, and θ denote the irradiation wavelength, half-maximum peak width, and diffraction angle of the diffraction peak under inspection, respectively. Moreover, k denotes the Scherrer constant with a value of 0.94. It is worth noting that the intensities of characteristic diffraction signals of the fabricated samples follow the order $BiVO_4$-C {−121} < $BiVO_4$-R {−121} < $BiVO_4$-H {−121}. However, the {040}/{110} diffraction signal intensity ratio is shown to be elevated in $BiVO_4$-R relative to $BiVO_4$-C and $BiVO_4$-H, suggesting superior growth of $BiVO_4$ crystals vertical to the {110} facets.[33] This was further attested by FESEM analysis. Moreover, a minor variation in fwhm value was observed, which suggests the existence of a minor distortion of the [VO_4^{-3}] tetrahedron in the local structure.[26]

Furthermore, broad and readily distinguishable characteristic ν_3 stretching vibrational absorption spectra were observed in the range of 1000 to 500 cm^{-1} in FT-IR analyses of fabricated $BiVO_4$ samples (Figure 2b). The characteristic signals at around 739 and 838 cm^{-1} are well-attributed to ν_3 asymmetric and ν_1 symmetric stretching vibrational modes of the VO_4^{3-} unit, respectively.[42] Moreover, a weak signal around 474 cm^{-1} was observed and ascribed to the ν_4 bending vibrational mode of VO_4^{3-}.[43] This is in good agreement with the monoclinic scheelite phase of $BiVO_4$ samples.

Furthermore, the valence band of monoclinic scheelite $BiVO_4$ is reported to be composed of Bi_{6s} and O_{2p} hybrid orbitals, while the conduction band is composed of a V_{3d} orbital.[11,23] The existence of distortion of the VO_4^{3-} tetrahedron in the local structure along with superior crystallinity is responsible for escalating the overlap of Bi_{6s} and O_{2p} orbitals of monoclinic scheelite $BiVO_4$. This consequently enhanced the photoexciton delocalization process and enhanced the migration of photogenerated holes to the surface, accordingly resulting in a superior water oxidation reaction.[24,26] Thus, when the X-ray diffraction facts

https://dx.doi.org/10.1021/acs.inorgchem.0c01465
Inorg. Chem. 2020, 59, 10328−10342

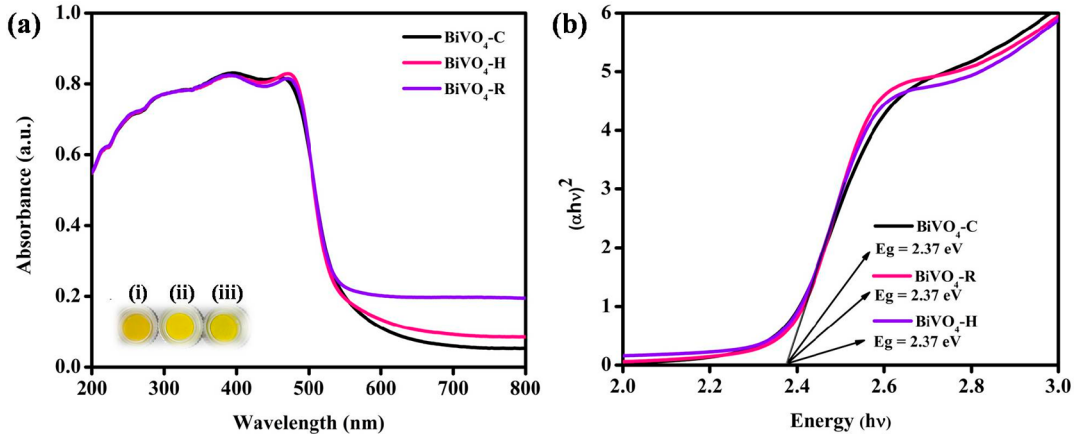

Figure 4. (a) UV−vis DRS spectra and (b) Tauc plots of fabricated monoclinic scheelite $BiVO_4$ samples.

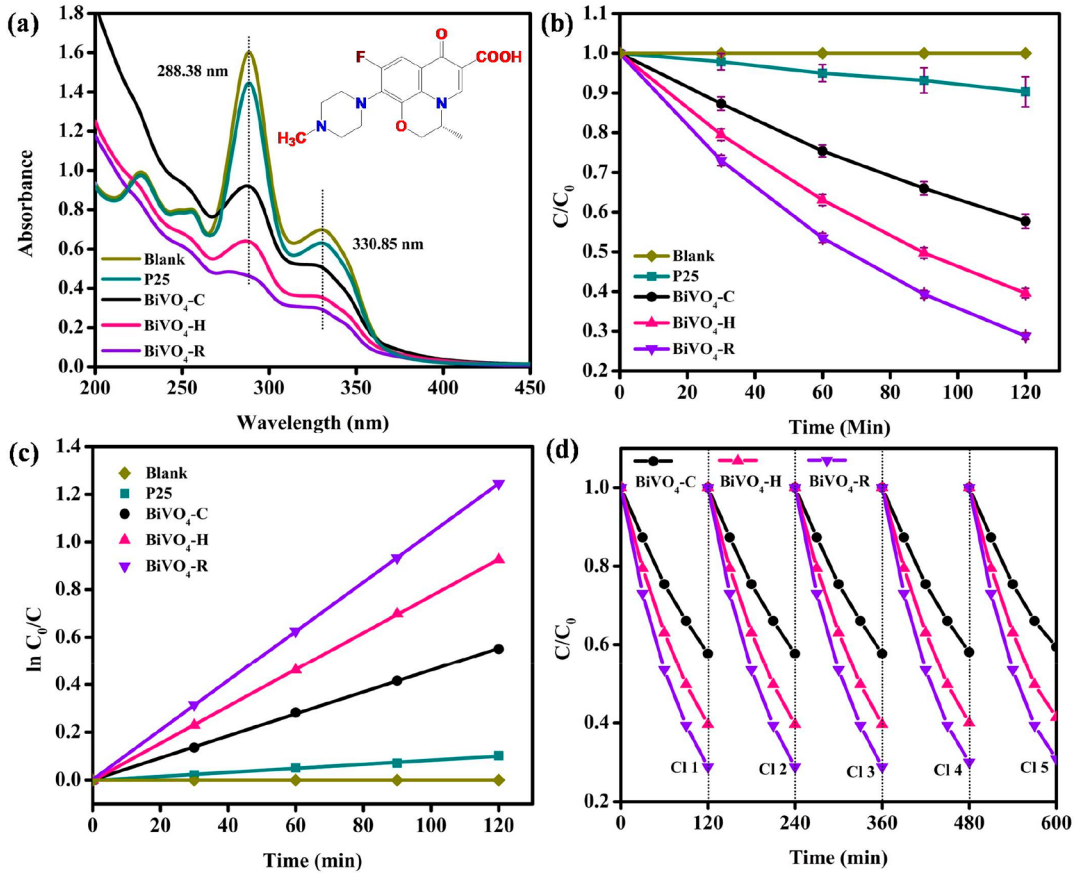

Figure 5. (a) UV−vis absorption spectrum of levofloxacin undergoing photodetoxification, (b) detoxification over time, (c) kinetics of detoxification, and (d) cyclic reusability measurements over fabricated monoclinic scheelite $BiVO_4$ samples.

are taken into account, the higher crystallinity of $BiVO_4$-H attests to its superior photocatalytic redox activity over $BiVO_4$-R and $BiVO_4$-C sequentially. This was further supported by the crystallite sizes of fabricated catalysts. The larger crystallite size of $BiVO_4$-H suggests a higher photocatalytic activity in comparison to $BiVO_4$-R and $BiVO_4$-C.[24,26]

XPS measurements of fabricated hierarchical structures of the $BiVO_4$ material were carried out to thoroughly investigate the surface elemental composition and valence states (Figure 3). The XPS survey spectrum of fabricated $BiVO_4$ materials illustrates the presence of Bi, V, and O devoid of any adulteration (Figure 3a). The appearance of an intense XPS signal of C near 284.9 eV was readily attributed to the adventitious hydrocarbon.[11,12] Two prominent XPS signals are observed for Bi 4f narrow scan spectrum for the fabricated $BiVO_4$-C (159.12, 164.42 eV), $BiVO_4$-H (159.14, 164.42 eV), and $BiVO_4$-R (159.17, 164.46 eV) materials. The observed binding energy differences of 5.3, 5.28, and 5.29 eV are due to the respective Bi $4f_{7/2}$ and Bi $4f_{5/2}$ spin−orbit splitting and +3 state of the Bi atom (Figure 3b).[11,12] The characteristic spin−orbit splitting of V $2p_{3/2}$ and V $2p_{1/2}$ were observed for fabricated $BiVO_4$-C (516.51, 523.77 eV), $BiVO_4$-H (516.51, 523.93 eV) and $BiVO_4$-R (516.52, 523.75 eV) materials with binding energy differences of 7.26, 7.42, and 7.23 eV,

https://dx.doi.org/10.1021/acs.inorgchem.0c01465
Inorg. Chem. 2020, 59, 10328−10342

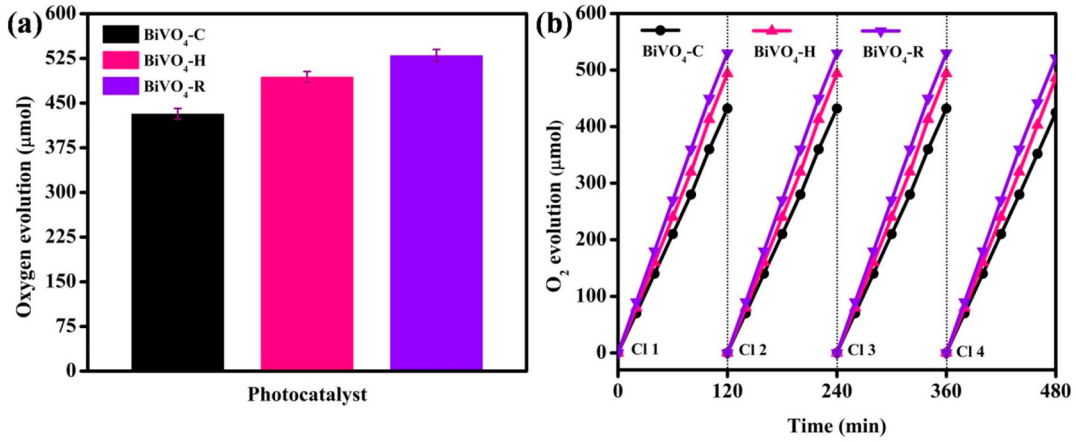

Figure 6. Comparative (a) O_2 evolution and (b) cyclic reusability measurements over fabricated monoclinic scheelite $BiVO_4$ samples.

respectively, ascribed to the +5 valence state of the vanadium atom (Figure 3c).[11,12] Moreover, the O 1s XPS spectra of fabricated $BiVO_4$-C (529.57, 531.28 eV), $BiVO_4$-H (529.59, 531.34 eV), and $BiVO_4$-R (529.59, 531.28 eV) materials illustrate a pair of intense signals corresponding to lattice oxygens of Bi−O and V−O bonds (lower BE energy) and hydroxyl oxygen (−OH) (higher BE energy) (Figure 3d).[22] The results illustrate the existence of a $BiVO_4$ material with a monoclinic scheelite crystalline phase.

The strong optoelectronic response of the pristine $BiVO_4$ catalysts with strapping (strong) absorption characteristic in visible region was well exposed by UV−vis diffuse reflectance spectroscopy (Figure 4a). The observed absorption edges were devoid of significant differences with approximate values of nearly 551−554 nm for $BiVO_4$-C, $BiVO_4$-H, and $BiVO_4$-R, respectively, with a trifling red shift of $BiVO_4$-C in comparison to the other pristine catalysts.[33] The observed absorption characteristics were consistent with the closely analogous colors of fabricated (i) $BiVO_4$-C, (ii) $BiVO_4$-H, and (iii) $BiVO_4$-R samples (Figure 4a, inset). Moreover, the absorption edges were projected to originate from respective optical band-gap transitions rather than from any impurity levels. The close band-gap values were estimated by implementing eq 9:[11,16,44]

$$\alpha h\nu = A(h\nu - E_g)^{n/2} \tag{9}$$

Here, α, h, A, ν, and E_g denote the absorption coefficient, Planck's constant, the proportionality constant, light frequency, and band-gap energy, respectively. The value of n was adopted as 1 for the direct transition natures of fabricated samples.[11,16] The probable close band-gap energies were observed to have no apparent divergences and evaluated to be 2.37 eV for $BiVO_4$-C, $BiVO_4$-H, and $BiVO_4$-R ,respectively (Figure 4b), which are in accordance with the absorption analysis and previous reports.[11,28] Moreover, the light-harvesting efficiency was proposed to have no effective association toward the diverse photocatalytic efficiencies of fabricated shape-selective $BiVO_4$ materials.

Furthermore, a comparison of the photoredox efficiencies of the fabricated catalysts were investigated by performing degradation of an organic deleterious waste levofloxacin ($C_{18}H_{20}FN_3O_4$) aqueous solution over 120 min of visible light illumination. For a comparative illustration commercial-grade Degussa P25 was also introduced. A drastic decrease in the respective signal intensities for aromatic (288.38 nm) and piperazine (330.85 nm) rings in the UV−vis absorption spectrum evidenced the photocatalytic degradation process (Figure 5a, inset).[23,35] Negligible detoxification results were observed for Degussa P25, while roughly no degradation was observed for a solution lacking a catalyst (photolysis). The degradation percentages of levofloxacin were evaluated to be 42.3%, 60.4%, and 71.2% for $BiVO_4$-C, $BiVO_4$-H, and $BiVO_4$-R, respectively. Moreover, the detoxification was well observed by employing a pseudo-first-order kinetic model (Figure 5b,c) and the detoxification rate constant was evaluated adopting eq 10:[11,17]

$$\ln(C/C_0) = -kt \tag{10}$$

Here, C, C_0, k, and t denote the final concentration, the initial concentration, the rate constant, and the reaction time, respectively. A higher rate constant for $BiVO_4$-R (0.0104 min^{-1}) was apparent, which is 1.35- and 2.24-fold superior to those of the fabricated $BiVO_4$-H (0.0077 min^{-1}) and $BiVO_4$-C (0.0046 min^{-1}) samples.

Cyclic reuses of fabricated $BiVO_4$ hierarchical micro-structures were carried out to investigate the apparent photostability and recyclability (Figure 5d). The detoxification was observed to be consistent up to four consecutive cycles with minimal deteriorations of 1.82%, 1.86%, and 2.03% in the fifth cycle for $BiVO_4$-C, $BiVO_4$-H, and $BiVO_4$-R, respectively, ascribed to the wear and tear of the catalyst surface and inevitable losses during the intermediary recovery process.[11,12,22]

In addition, photocatalytic oxygen evolution efficiencies of fabricated samples were carried out in $AgNO_3$ aqueous solution under visible-light illumination for 120 min. Expectedly, $BiVO_4$-R illustrated an elevated water oxidation efficiency of 530.6 μmol, which was about 1.22 and 1.07 times those of $BiVO_4$-C (434.2 μmol) and $BiVO_4$-H (494.8 μmol), respectively (Figure 6a). Cyclic reuses of the fabricated hierarchical $BiVO_4$-R sample showed significant steadiness up to three successive cycles followed by deteriorations of 1.64%, 1.58%, and 1.62% in the fourth cycle for $BiVO_4$-C, $BiVO_4$-H, and $BiVO_4$-R, respectively. The inconsistency observed was ascribed to the wear and tear of the catalyst surface over the reaction period. Moreover, the inescapable metallic Ag cluster deposition owing to photoreduction of Ag^+ ions over the catalyst surface consequently hinders visible light penetration, thus retarding the activity (Figure 6b).[11,12,22] The diverse photocatalytic response was credited to varied photo electron−

https://dx.doi.org/10.1021/acs.inorgchem.0c01465
Inorg. Chem. 2020, 59, 10328−10342

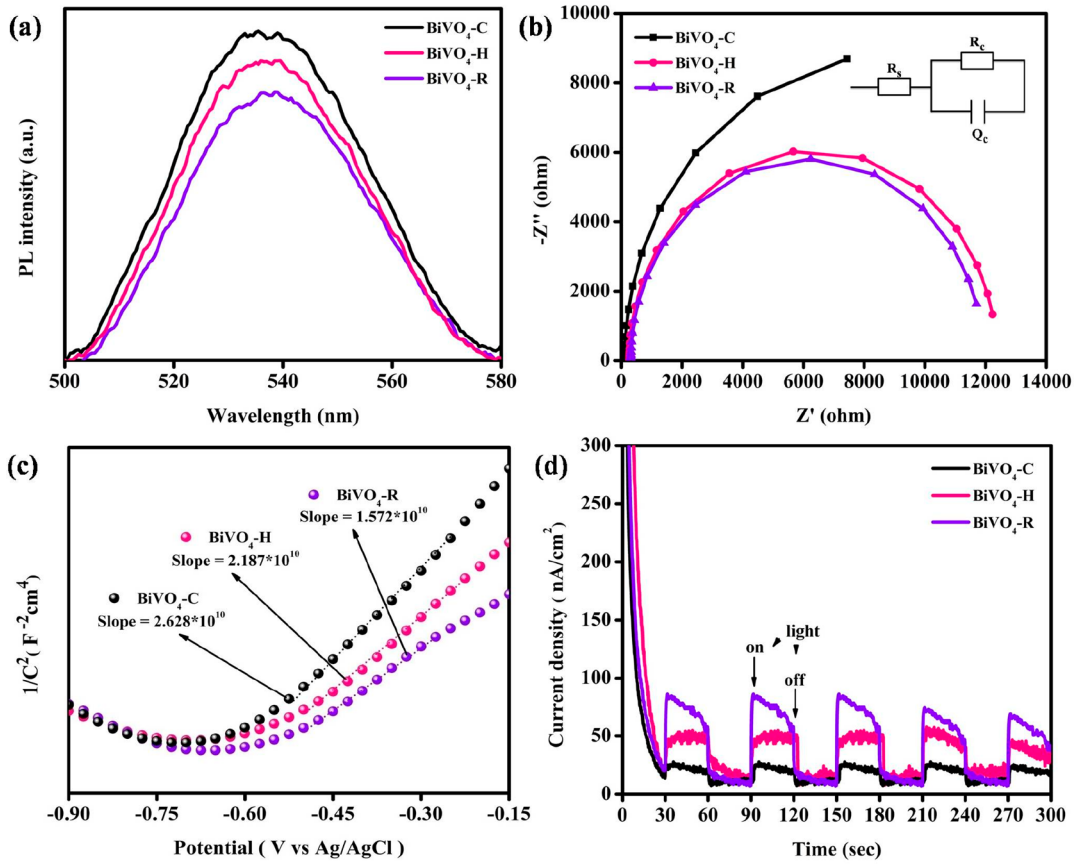

Figure 7. (a) PL, (b) EIS, (c) carrier density, and (d) transient photocurrent responses of fabricated monoclinic scheelite $BiVO_4$ samples.

hole anti-recombination processes occurring in the crystal microstructures and was well-explored via photoelectrochemical measurements.

Moreover, a detailed investigation regarding photoexciton separation, migration, and recombination in the fabricated materials was well established via PL analysis (λ_{ex} = 325 nm, room temperature). As shown in Figure 7a, the broad PL spectra of the fabricated catalysts are centered at 536 nm and are ascribed to the corresponding band-gap emissions.[11,27] Expectedly, PL intensities of the catalysts had minimal differences. Nevertheless, $BiVO_4$-R has a comparatively lower PL intensity followed by $BiVO_4$-H and $BiVO_4$-C, suggesting lower charge carrier recombination rates.[11,27] This was further corroborated by the electrochemical impedance analysis shown in Figure 7b. The exposed characteristic semicircular Nyquist plots validate the occurrence of exciton separation and transfer in fabricated samples.[11,45] Moreover, a comparatively low frequency and smaller arc radius confirms an effective decrease in interfacial charge transfer resistance (R_c) in the fabricated $BiVO_4$-R microstructure in comparison to the pristine $BiVO_4$-C and $BiVO_4$-H. However, the variation was minimal in comparison to $BiVO_4$-H. The fitted Randle circuit model further validates a notable decrease in charge transfer resistance over the electrode−electrolyte interface of $BiVO_4$-R (11620 Ω cm^{-2}) relative to $BiVO_4$-C (17640 Ω cm^{-2}) and $BiVO_4$-H (12120 Ω cm^{-2}) and thus illustrates possible superior charge carrier migration in architected $BiVO_4$-R relative to $BiVO_4$-C and $BiVO_4$-H samples. R_s and Q_c elements (Figure 7b, inset) in the equivalent circuit denote series resistance and capacitance phase elements, respectively.[11,45,46] Moreover, a lower positive slope was observed for $BiVO_4$-R (1.572×10^{10}) relative to $BiVO_4$-H (2.187×10^{10}) and $BiVO_4$-C (2.628×10^{10}) sequentially (Figure 7c). This further indicates a higher carrier density (N_d) and thus elevated electrical conductance provoking the superior charge-transfer characteristics of $BiVO_4$-R in comparison to the fabricated $BiVO_4$-C and $BiVO_4$-H samples. Moreover, the probable values of carrier densities (N_d) of fabricated $BiVO_4$ samples could be calculated by adopting eq 11:[11,46−50]

$$\text{carrier density } (N_d) = (2/e\varepsilon\varepsilon_0)B \tag{11}$$

Here, e, ε, ε_0, and B denote the electron charge (1.602×10^{-19} C), the relative dielectric constant of the semiconducting material, the vacuum permittivity (8.85×10^{-12} F m^{-1}), and the slope value of MS plot tangents, respectively. Consequently, an increased carrier concentration will lead to elevated charge-transfer characteristics of $BiVO_4$ as per eq 12:[50]

$$\text{electrical conductivity } (\sigma) = en\mu \tag{12}$$

Here, e, n, and μ denote the electronic charge unit (1.602×10^{-19} C), the charge carrier concentration, and the charge carrier mobility, respectively.

Moreover, the photoelectrochemical transient measurements illustrated an enhanced transient photocurrent intensity of $BiVO_4$-R (Figure 7d). The results were observed to follow the trend of $BiVO_4$-C < $BiVO_4$-H < $BiVO_4$-R for each consecutive on−off cycle, suggesting an improved exciton pair separation tendency and surface charge antirecombination process over $BiVO_4$-R in comparison to the other pristine materials.[11,22,51]

https://dx.doi.org/10.1021/acs.inorgchem.0c01465
Inorg. Chem. 2020, 59, 10328−10342

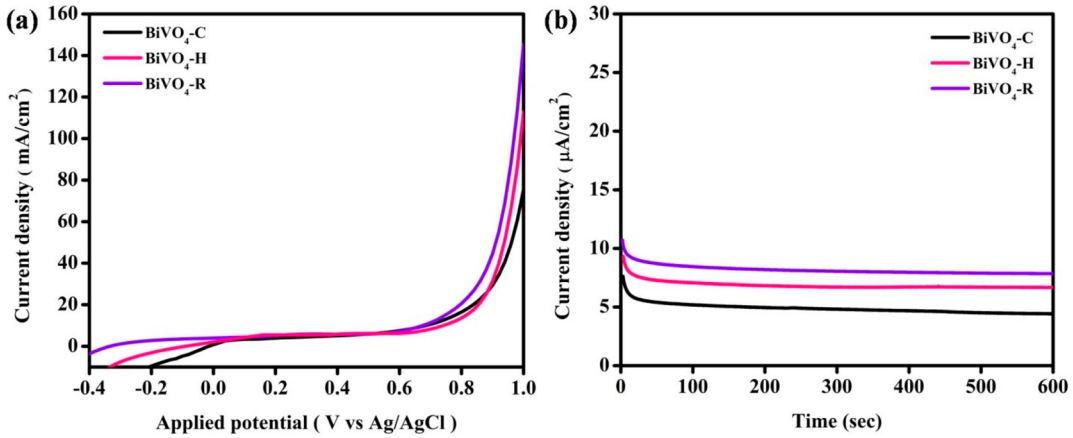

Figure 8. Comparative (a) LSV and (b) CA analysis responses of fabricated monoclinic scheelite $BiVO_4$ samples.

Moreover, linear sweep voltammograms (LSV) exposing a higher photocurrent density of $BiVO_4$-R (145.6 $\mu A/cm^2$) relative to $BiVO_4$-C (75.5 $\mu A/cm^2$) and $BiVO_4$-H (113.1 $\mu A/cm^2$) validates the sturdy charge carrier separation occurring over $BiVO_4$-R. Nevertheless, a drastic reduction in charge carrier recombination was validated by a notable negative shift in onset potential for $BiVO_4$-R (−0.33 V) in comparison to the fabricated $BiVO_4$-C (−0.013 V) and $BiVO_4$-H (−0.11 V).[51] The result is in good agreement with PL, impedance, carrier density, and transient photocurrent analysis (Figure 8a).

The time-variant photocurrent steadiness of the fabricated $BiVO_4$ materials was investigated by chronoamperometric analysis (Figure 8b). Expectedly, $BiVO_4$-R illustrated an enhanced CA current of 7.9 μA with consistency up to 600 s. Following a minimal decay of 25.2% initially, there was no noticeable photocurrent loss observed over time, suggesting an enhanced electron lifetime in the $BiVO_4$-R sample in comparison to $BiVO_4$-C and $BiVO_4$-H. Moreover, the measured CA results followed the trend $BiVO_4$-C (42%, 4.52 μA) < $BiVO_4$-H (28%, 6.7 μA) < $BiVO_4$-R. The diverse photoelectrochemical responses were quite consistent with the observed photocatalytic outcomes.

Furthermore, a Bode analysis was executed to better understand the hole relaxation efficiencies of fabricated samples. A relatively positive shift of the frequency phase peak of $BiVO_4$-H in comparison to $BiVO_4$-R and $BiVO_4$-C as projected in Bode plots reveals a decrease in hole separation/relaxation lifetime (τ_p) for $BiVO_4$-H in comparison to the other pristine phases (Figure 9). Moreover, the entire separation/relaxation lifetimes in the fabricated $BiVO_4$ samples were evaluated to be 0.91, 0.48, and 0.61 ms for $BiVO_4$-C, $BiVO_4$-H, and $BiVO_4$-R, respectively, adopting eq 13:[51−54]

$$\text{hole relaxation lifetime } (\tau_p) = 1/2\pi f \tag{13}$$

Here, f denotes the relaxation frequency obtained from the maximum value allied with the Bode frequency range. A decrease in hole relaxation lifetime suggests a decrease in hole diffusion length (L_D) and thus a rapid hole diffusion process. The diffusion lengths were evaluated to be 2.17, 1.57, and 1.78 μm for $BiVO_4$-C, $BiVO_4$-H, and $BiVO_4$-R, respectively, adopting eq 14:[51−54]

$$\text{hole diffusion length } (L_D) = (D\tau_p)^{1/2} \tag{14}$$

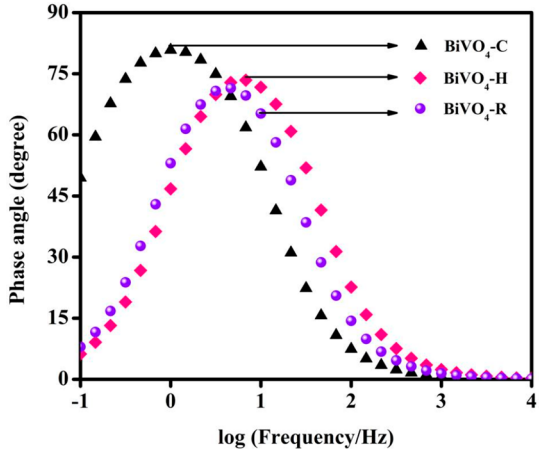

Figure 9. Bode analysis results of fabricated monoclinic scheelite $BiVO_4$ samples.

Here, D connotes the hole diffusion coefficient with a value of 5.2×10^{-2} cm^2 s^{-1}.[24] A reasonably lower hole diffusion length of $BiVO_4$-H (1.57 μm) in comparison to $BiVO_4$-C (2.17 μm) and $BiVO_4$-R (1.78 μm) was observed, suggesting a superior hole consumed water decomposition reaction of $BiVO_4$-H relative to $BiVO_4$-R and $BiVO_4$-C sequentially.[24−26] This was further supported by crystallographic parameters and comparatively higher amounts of exposed {110} oxidation facets of the $BiVO_4$-H sample.[31,37] However, the constructive effects of the {040/110} facet isotype heterojunction and exposure ratio of various reduction−oxidation facets of monoclinic scheelite $BiVO_4$ were investigated to regulate the overall efficiencies of the catalysts.

As revealed by FESEM and TEM analysis, the fabricated $BiVO_4$-C is devoid of any good exposure extent, while $BiVO_4$-H and $BiVO_4$-R samples have well-exposed {040} reduction and {110} oxidation facets and built-in {040/110} facet isotype heterojunctions.[27−29] With no perceptible exposed redox facets, $BiVO_4$-C suffers rapid exciton recombination (Scheme 3a). As revealed from XRD, FESEM, and TEM analysis, the {040/110} exposure factor in $BiVO_4$-H is noticeably lower relative to $BiVO_4$-R. Reasonably more exposed and energetically favorable water oxidation {110} facets suggest higher hole provoked efficiency of $BiVO_4$-H; however, recombination occurring due to trapped electrons owing to minor exposed {040} facets decrease the activity

https://dx.doi.org/10.1021/acs.inorgchem.0c01465
Inorg. Chem. 2020, 59, 10328−10342

Scheme 3. Graphics of Photoexciton Separation/Recombination Phenomena over (a) $BiVO_4$-C and (b) $BiVO_4$-H {040/110} Facet Isotype Heterojunctions and (c) Mechanistic Pathway of Exciton Separation over a $BiVO_4$-R {040/110} Facet Isotype Heterojunction with Photocatalytic (I) Levofloxacin Detoxification and (II) Water Oxidation

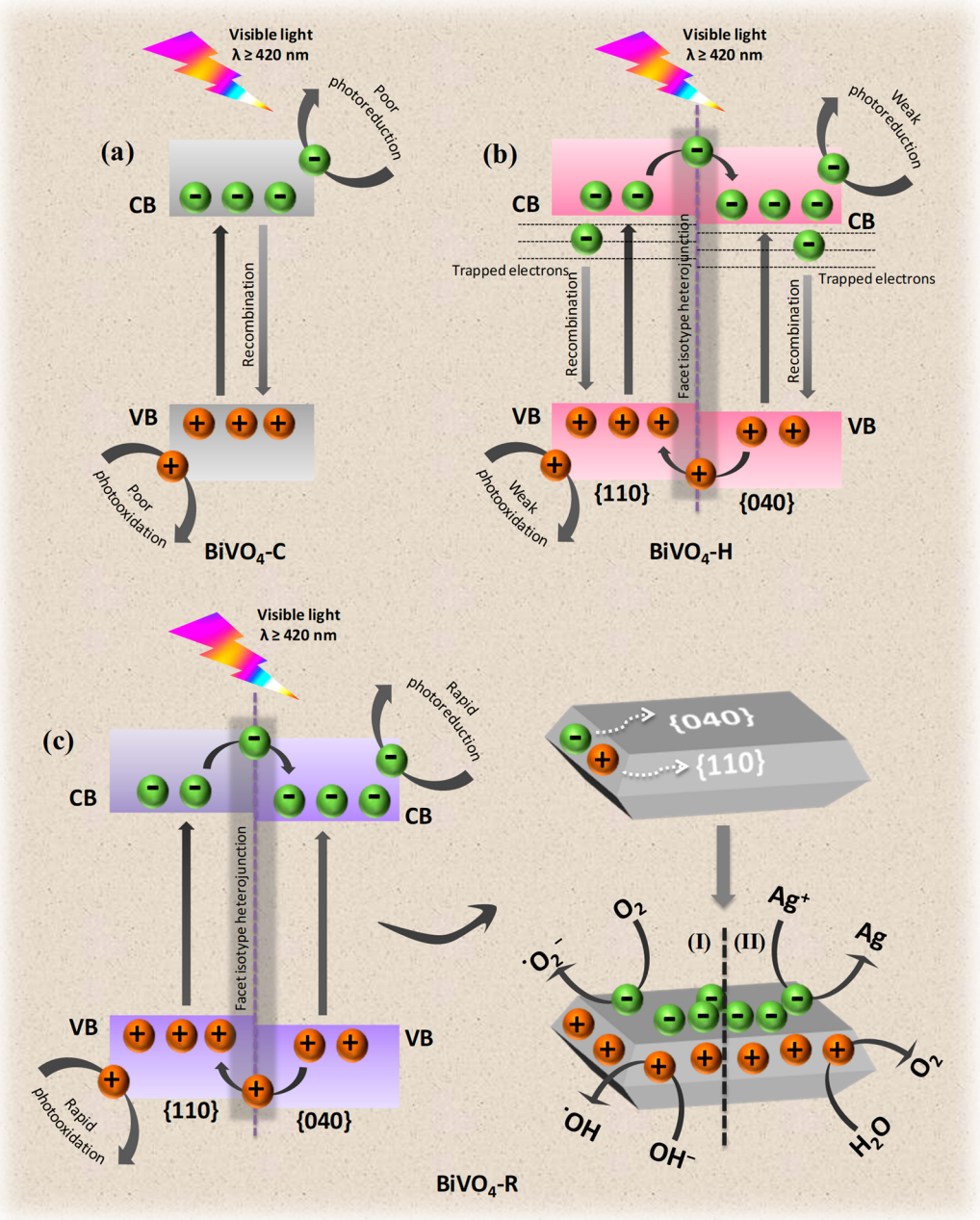

(Scheme 3b).[31] Moreover, a higher {110} facet exposure causes an electron overflow effect provoked retardation of electron transfer to the {040} facet and thus validates the existence of interior exciton pair recombination.[39]

In contrast, highly exposed {040} facets have been reported to possess a superior water molecule adsorption efficiency due to the promotion of the local bonding configuration along with the presence of multiatomic BiV_4 centers responsible for electron transfer for water oxidation (Scheme 3c).[29,55] Thus, an increase in the relative exposure factor of {040} facet ({040}/{110}), i.e. a greater exposed {040} exposure percentage, possesses a constructive effect toward exciton separation and anti-recombination processes over {040/110} facet isotype heterojunctions and hence superior photocatalytic activity.[33,38,56] Consequently, the phenomenon results in an enhanced effective separation of photoexcitons and redox efficiency over $BiVO_4$-R in comparison to $BiVO_4$-H and $BiVO_4$-C, which is in good agreement with the results of photocatalytic and photoelectrochemical measurements.

Furthermore, the inbuilt {040/110} facet isotype heterojunction provoked augmented accumulation of photoelectrons over the {040} reduction facet of $BiVO_4$-R was further evidenced by introducing Ag nanoparticles via a photodeposition method. A powder XRD spectrum of the Ag-$BiVO_4$-R sample shows the existence of {111} and {200} crystal plane reflections (JCPDS 00-001-1167), which suggests

https://dx.doi.org/10.1021/acs.inorgchem.0c01465
Inorg. Chem. 2020, 59, 10328−10342

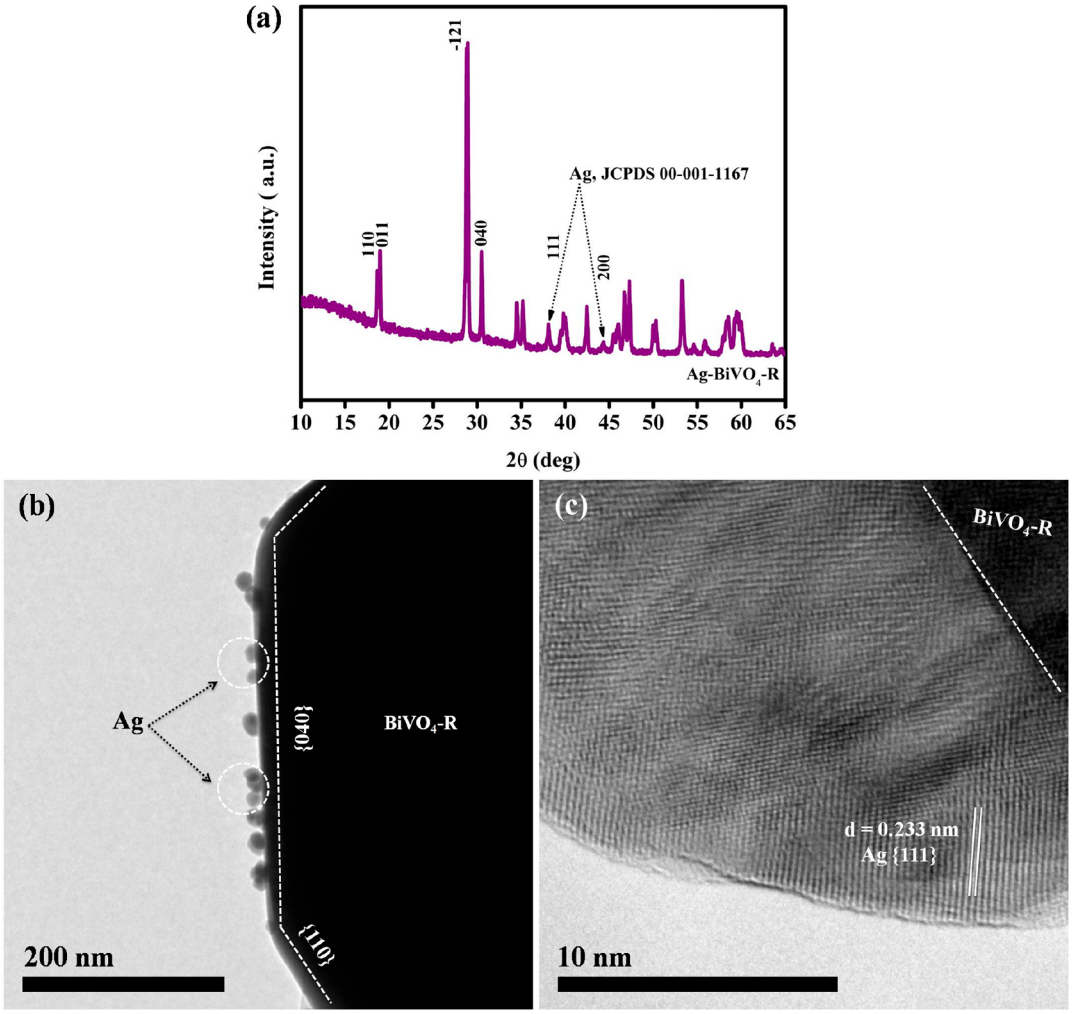

Figure 10. (a) XRD, (b) TEM, and (c) HRTEM results of the fabricated Ag-$BiVO_4$-R sample.

successful integration of metallic Ag with the $BiVO_4$-R sample (Figure 10a). A low-magnification TEM image of Ag-$BiVO_4$-R illustrates the augmented deposition of Ag nanoparticles over the {040} crystal facet of $BiVO_4$-R (Figure 10b). An observed interplanner spacing (d) of 0.233 nm was allied with the reflection of the {111} plane of metallic silver nanoparticles (Figure 10c). The deposition was ascribed to rapid-selective photoreduction of Ag^+ particles to Ag^0 via augmented photoelectrons accumulating over the {040} reduction facet of the $BiVO_4$-R {040/110} facet isotype heterojunction. The possible mechanistic pathway for the photodeposition is as follows:[27,29,30]

$$\{040/110\}\text{-}BiVO_4\text{-R} + h\nu \rightarrow \{040\}\text{-}BiVO_4\text{-R}\ e^- + \{110\}\text{-}BiVO_4\text{-R}\ h^+ \quad (15)$$

$$\{040\}\text{-}BiVO_4\text{-R}\ e^- + Ag^+ \rightarrow Ag^0\text{-}\{040\}\text{-}BiVO_4\text{-R} \quad (16)$$

A Mott–Schottky analysis was adopted to evaluate the probable conduction band edge potentials and charge-transfer characteristics of the fabricated monoclinic scheelite $BiVO_4$ samples (Figure 11a). The probable flat-band potentials (E_{fb}) were calculated to be −0.71, −0.68, and −0.63 V vs Ag/AgCl for $BiVO_4$-C, $BiVO_4$-H, and $BiVO_4$-R, respectively, from the x intercept of the extrapolated linear region of the C^{-2} versus potential plot employing eq 17.[56] Moreover, the relatively positive shift in the flat band potential of $BiVO_4$-R suggests a minor electron-trapping process and thus an effectual lowering of photoelectron diffusion length from the bulk to the well-exposed {040} surface.[31]

$$1/C^2 = (2/e\varepsilon\varepsilon_0 N_d)[E - E_{fb} - (kT/e)] \quad (17)$$

Here, C, e, ε, ε_0, N_d, E, and E_{fb} denote the charge capacitance of free space, the charge of the elementary electron, the dielectric constant of the electrode material, the permittivity of free space, the electron donor density, the applied bias potential, and the flat band potential, respectively. Moreover, n-type characteristics of fabricated monoclinic $BiVO_4$ materials were well attested from positive slopes in the MS plot and probable conduction band (CB) values were calculated to be −0.15, −0.12, and −0.07 eV vs NHE for $BiVO_4$-C, $BiVO_4$-H, and $BiVO_4$-R, respectively. The result was due to the fact that E_{fb} of n-type materials gives an approximation of the conduction band minimum.[11,57] Nevertheless, the valence band (VB) edges were evaluated to be 2.22, 2.25, and 2.30 eV vs NHE for $BiVO_4$-C, $BiVO_4$-H, and $BiVO_4$-R, respectively, adopting eq 18:[58]

$$E_{CB} = E_{VB} - E_g \quad (18)$$

Here, E_{CB}, E_{VB}, and E_g denote the CB minimum, VB maximum, and band-gap energy, respectively. The relative

https://dx.doi.org/10.1021/acs.inorgchem.0c01465
Inorg. Chem. 2020, 59, 10328−10342

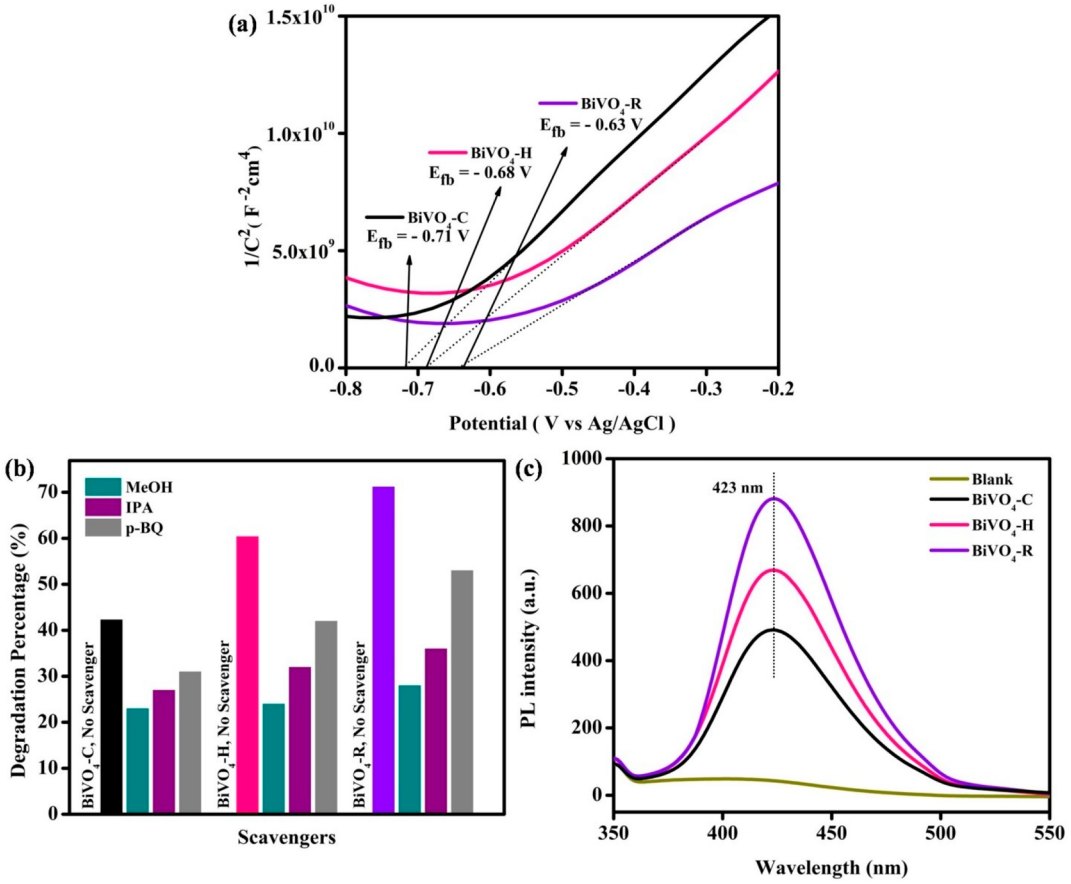

Figure 11. (a) Mott–Schottky, (b) active radical measurement, and (c) TA plots of fabricated monoclinic scheelite $BiVO_4$ samples.

variations in band edge potential (CB and VB) values of fabricated $BiVO_4$ materials are due to diverse facet exposure factors, as the surface atomic coordinations and arrangements of different exposed facets are different.[59] The evaluated probable near band edge structures of the fabricated samples with relative potentials of various components accountable for photocatalytic redox reactions are shown in Scheme 4.

Scheme 4. Schematic Illustration of near Possible Band Structures of Fabricated Monoclinic Scheelite $BiVO_4$ Samples

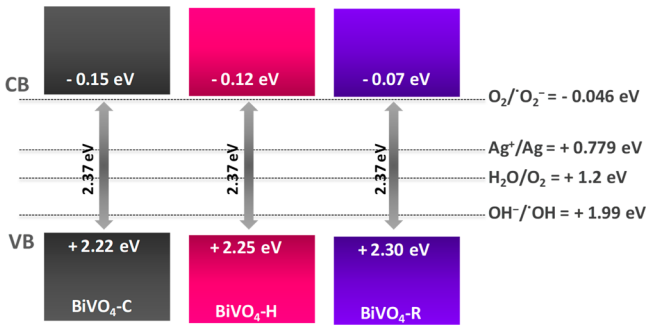

Moreover, the effective association of various active radicals and thus possible inherent mechanistic pathways involved in the detoxification process of levofloxacin were elucidated via sequential scavenging experiments. In the present investigation, h^+, $\dot{O}H$, and O_2^- active species are well trapped via the introduction of methanol (MeOH), isopropyl alcohol (IPA), and *p*-benzoquinone (p-BQ) as scavenging agents, respectively (Figure 11b).[11,12,22] As was observed, all three $BiVO_4$ samples with hierarchical morphologies demonstrate analogous outcomes. The detoxification was strappingly (strongly) hindered upon scavenging h^+ and grounds (results) a lowering of detoxification to 23, 24, and 28% associated with $BiVO_4$-C, $BiVO_4$-H, and $BiVO_4$-R, respectively. Moreover, scavenging $\dot{O}H$ radicals significantly decreases the degradation to 27, 32, and 36% associated with $BiVO_4$-C, $BiVO_4$-H, and $BiVO_4$-R, respectively. However, $\cdot O_2^-$ makes a relatively lower contribution toward the degradation process and this is well-observed from a comparatively poorer decrease in degradation to 31, 42, and 53% for $BiVO_4$-C, $BiVO_4$-H, and $BiVO_4$-R, respectively. The results illustrate the involvement of each of the active radicals in the degradation process of LVF with a crucial contribution of h^+ and $\dot{O}H$ radicals. Moreover, a significant association of $\dot{O}H$ radical was further validated from the considerable increase in PL intensity owing to the transformation of terephthalic acid (TA, 423 nm) to fluorescent hydroxyterephthalic acid (HTA) by the excess $\dot{O}H$ radicals produced.[60] The results follow the trend $BiVO_4$-C < $BiVO_4$-H < $BiVO_4$-R, suggesting enhanced exciton pair separation over the $BiVO_4$-R sample (Figure 11c).[61] The results were in good agreement with the band configurations of fabricated samples and previous reports (Scheme 4).[34−36,61]

In this context, a credible mechanistic pathway was projected to better explain the photoredox phenomenon over $BiVO_4$-R. The inherent {040/110} facet isotype heterojunction promotes the augmented accumulation of photoexcited electrons over {040}-$BiVO_4$-R with a lower conduction band

https://dx.doi.org/10.1021/acs.inorgchem.0c01465
Inorg. Chem. 2020, 59, 10328−10342

potential and photogenerated holes over {110}-$BiVO_4$-R with a lower valence band potential, respectively.[29,33] Meticulously, the holes over the $BiVO_4$-R {110} facet actively oxidize OH^- to produce an $^{\bullet}OH$ radical ($OH^-/^{\bullet}OH$ = +1.99 eV), while electrons over the $BiVO_4$-R {040} facet react with dissolved O_2 to produce the $^{\bullet}O_2^-$ radical ($O_2/^{\bullet}O_2^-$ = −0.046 eV). The h^+, $^{\bullet}OH$, and $^{\bullet}O_2^-$ radical subsequently instigate the detoxification of levofloxacin (Scheme 3c-I).[34,35] On the other hand, the excess electrons over the $BiVO_4$-R {040} facet with high reduction potential actively reduce Ag^+ to form metallic Ag (Ag^+/Ag^0 = +0.779 eV). Consequently, the active holes over the $BiVO_4$-R {110} facet rapidly oxidize H_2O to O_2 (H_2O/O_2 = +1.2 eV) (Scheme 3c-II).[11,12]

(I) Possible levofloxacin degradation pathway:

$$\{040/110\}\text{-}BiVO_4\text{-R} + h\nu_{vis} \rightarrow \{040\}\text{-}BiVO_4\text{-R}\ e^- + \{110\}\text{-}BiVO_4\text{-R}\ h^+ \quad (19)$$

$$\{040\}\text{-}BiVO_4\text{-R}\ e^- + O_2 \rightarrow {}^{\bullet}O_2^- \quad (20)$$

$$\{110\}\text{-}BiVO_4\text{-R}\ h^+ + OH^- \rightarrow {}^{\bullet}OH \quad (21)$$

$$h^+ + \text{LVF} \rightarrow \text{degradation product (major)} \quad (22)$$

$$^{\bullet}OH + \text{LVF} \rightarrow \text{degradation product (major)} \quad (23)$$

$$^{\bullet}O_2^- + \text{LVF} \rightarrow \text{degradation product} \quad (24)$$

(II) Possible water oxidation pathway:

$$\{040/110\}\text{-}BiVO_4\text{-R} + h\nu_{vis} \rightarrow \{040\}\text{-}BiVO_4\text{-R}\ e^- + \{110\}\text{-}BiVO_4\text{-R}\ h^+ \quad (25)$$

$$AgNO_3 + h\nu_{vis} \rightarrow Ag^+ + NO_3^- \quad (26)$$

$$\{040\}\text{-}BiVO_4\text{-R}\ e^- + Ag^+ \rightarrow \{040\}\text{-}BiVO_4\text{-R} + Ag^0 \quad (27)$$

$$\{110\}\text{-}BiVO_4\text{-R}\ h^+ + H_2O \rightarrow \{110\}\text{-}BiVO_4\text{-R} + O_2 + H^+ \quad (28)$$

4. CONCLUSION

In summary, highly crystalline hierarchical microstructures of monoclinic scheelite $BiVO_4$ were fabricated via varied synthetic courses and were well established by analytical characterizations. An Annona reticulate-shaped $BiVO_4$ was obtained by a calcination ($BiVO_4$-C) treatment, while truncated bipyramidal morphologies with inbuilt {040/110} facet isotype heterojunctions were achieved by hydrothermal ($BiVO_4$-H) and reflux ($BiVO_4$-R) treatments. The photocatalytic redox efficiencies of the fabricated microstructures of $BiVO_4$ were well investigated over levofloxacin detoxification and the water oxidation reaction and actively compared. Superior exciton separation promoted enhanced photoactivity over the $BiVO_4$-R sample was exposed. The enhanced photoexciton antirecombination phenomenon was attributed to (i) well-exposed {040} reduction facet and {110} oxidation facet promoted facet isotype heterojunction formation and (ii) a high exposure percentage of {040} reduction facets of $BiVO_4$-R. The effect of physicochemical features, photoelectrochemical properties, {040/110} facet isotype heterojunctions, and relative exposure factors of oxidation−reduction facets toward the superior photocatalytic redox activity of $BiVO_4$ was well established. The findings are strongly promising and captivating toward the development of morphology and relative reduction−oxidation facet exposure factor selective fabrication of facet isotype heterojunction based materials for superior visible-active semiconductor photocatalysis.

AUTHOR INFORMATION

Corresponding Author

Kulamani Parida − *Centre for Nano Science and Nano Technology, Siksha 'O' Anusandhan (Deemed to be University), Bhubaneswar 751030, India;* orcid.org/0000-0001-7807-5561; Phone: +91-674-2421185; Email: paridakulamani@yahoo.com, kulamaniparida@soauniversity.ac.in; Fax: +91-674-2581637

Author

Basudev Baral − *Centre for Nano Science and Nano Technology, Siksha 'O' Anusandhan (Deemed to be University), Bhubaneswar 751030, India*

Complete contact information is available at: https://pubs.acs.org/10.1021/acs.inorgchem.0c01465

Notes

The authors declare no competing financial interest.

ACKNOWLEDGMENTS

The authors deeply acknowledge the Ministry of New and Renewable Energy (MNRE, 103/233/2014-NT), the Government of India, for financially assisting the research work. The authors also thank the SOA (Deemed to be University) for support and encouragement in publishing the work.

REFERENCES

(1) Hisatomi, T.; Kubota, J.; Domen, K. Recent advances in semiconductors for photocatalytic and photoelectrochemical water splitting. *Chem. Soc. Rev.* **2014**, *43*, 7520−7535.

(2) Huang, Z. F.; Pan, L.; Zou, J. J.; Zhang, X.; Wang, L. Nanostructured bismuth vanadate-based materials for solar-energy-driven water oxidation: a review on recent progress. *Nanoscale* **2014**, *6*, 14044−14063.

(3) Hojamberdiev, M.; Katsumata, K.; Morita, K.; Bilmes, S. A.; Matsushita, N.; Okada, K. One-step hydrothermal synthesis and photocatalytic performance of $ZnWO_4/Bi_2WO_6$ composite photocatalysts for efficient degradation of acetaldehyde under UV light irradiation. *Appl. Catal., A* **2013**, *457*, 12−20.

(4) Wu, R.; Song, H.; Luo, N.; Ji, G. Hydrothermal preparation of 3D flower-like $BiPO_4/Bi_2WO_6$ microsphere with enhanced visible-light photocatalytic activity. *J. Colloid Interface Sci.* **2018**, *524*, 350−359.

(5) Giannakopoulou, T.; Papailias, I.; Todorova, N.; Boukos, N.; Liu, Y.; Yu, J.; Trapalis, C. Tailoring the energy band gap and edges' potentials of $g\text{-}C_3N_4/TiO_2$ composite photocatalysts for NO_x removal. *Chem. Eng. J.* **2017**, *310*, 571−580.

(6) Dai, Z.; Qin, F.; Zhao, H.; Tian, F.; Liu, Y.; Chen, R. Time-dependent evolution of $Bi_{3.64}Mo_{0.36}O_{6.55}/Bi_2MoO_6$ heterostructure for enhanced photocatalytic activity via the interfacial hole migration. *Nanoscale* **2015**, *7*, 11991−11999.

(7) Wang, X.; Xu, Q.; Li, M.; Shen, S.; Wang, X.; Wang, Y.; Feng, Z.; Shi, J.; Han, H.; Li, C. Photocatalytic overall water splitting promoted by an $\alpha-\beta$ phase junction on Ga_2O_3. *Angew. Chem., Int. Ed.* **2012**, *51*, 13089−13092.

(8) Dong, F.; Zhao, Z.; Xiong, T.; Ni, Z.; Zhang, W.; Sun, Y.; Ho, W. K. In situ construction of $g\text{-}C_3N_4/g\text{-}C_3N_4$ metal-free heterojunction

for enhanced visible-light photocatalysis. *ACS Appl. Mater. Interfaces* **2013**, *5*, 11392−11401.
(9) Liang, Q.; Li, Z.; Bai, Y.; Huang, Z. H.; Kang, F.; Yang, Q. H. A composite polymeric carbon nitride with in situ formed isotype heterojunctions for highly improved photocatalysis under visible light. *Small* **2017**, *13*, 1603182.
(10) Kawahara, T.; Konishi, Y.; Tada, H.; Tohge, N.; Nishii, J.; Ito, S. A patterned TiO_2(Anatase)/TiO_2(Rutile) bilayer-type photocatalyst: effect of the anatase/rutile junction on the photocatalytic activity. *Angew. Chem., Int. Ed.* **2002**, *41*, 2811−2813.
(11) Baral, B.; Reddy, K. H.; Parida, K. M. Construction of M-$BiVO_4$/T-$BiVO_4$ isotype heterojunction for enhanced photocatalytic degradation of norfloxacine and oxygen evolution reaction. *J. Colloid Interface Sci.* **2019**, *554*, 278−295.
(12) Baral, B.; Mansingh, S.; Reddy, K. H.; Bariki, R.; Parida, K. M. Architecting double charge-transfer dynamics In_2S_3/$BiVO_4$ n-n isotype heterojunction for superior photocatalytic oxytetracycline hydrochloride degradation and water oxidation reaction: unveiling the association of physicochemical, electrochemical and photocatalytic properties. *ACS Omega* **2020**, *5*, 5270−5284.
(13) Cao, Y.; Li, Q.; Li, C.; Li, J.; Yang, J. Surface heterojunction between (001) and (101) facets of ultrafine anatase TiO_2 nanocrystals for highly efficient photoreduction CO_2 to CH_4. *Appl. Catal., B* **2016**, *198*, 378−388.
(14) Liu, N.; Chang, Y.; Feng, Y.; Cheng, Y.; Sun, X.; Jian, H.; Feng, Y.; Li, X.; Zhang, H. {101}-{001} Surface heterojunction-enhanced antibacterial activity of titanium dioxide nanocrystals under sunlight irradiation. *ACS Appl. Mater. Interfaces* **2017**, *9*, 5907−5915.
(15) Weng, S.; Fang, Z.; Wang, Z.; Zheng, Z.; Feng, W.; Liu, P. Construction of teeth like homojunction BiOCl (001) nanosheets by selective etching and Its high photocatalytic activity. *ACS Appl. Mater. Interfaces* **2014**, *6*, 18423−18428.
(16) Li, J.; Zhou, J.; Hao, H.; Li, W.; Liu, G. Exposed specific (040) and (110) facets of $BiVO_4$ modified with Bi_2WO_6 nanoparticles for enhanced photocatalytic performance. *New J. Chem.* **2017**, *41*, 6922−6927.
(17) Wang, P.; Zheng, J. Y.; Zhang, D.; Kang, Y. S. Selective construction of junctions on different facets of $BiVO_4$ for enhancing photo-activity. *New J. Chem.* **2015**, *39*, 9918−9925.
(18) Yang, J.; Peng, Y.; Chen, S.; Yang, B.; Liu, Y.; Peng, L.; Zhang, J. Controllable synthesis of $BiVO_4$ with a homojunction of (110) and (040) crystal facets for photocatalytic degradation of Rhodamine B. *Mater. Res. Express* **2019**, *6*, 085501.
(19) Zhang, Q.; Li, Z.; Wang, S.; Li, R.; Zhang, X.; Liang, Z.; Han, H.; Liao, S.; Li, C. The effect of redox cocatalysts location on photocatalytic overall water splitting over cubic $NaTaO_3$ semiconductor crystals exposed with equivalent facets. *ACS Catal.* **2016**, *6*, 2182−2191.
(20) Li, J.; Li, X.; Yin, Z.; Wang, X.; Ma, H.; Wang, L. Synergetic effect of facet junction and specific facet activation of $ZnFe_2O_4$ nanoparticles on photocatalytic activity improvement. *ACS Appl. Mater. Interfaces* **2019**, *11*, 29004−29013.
(21) Hao, X.; Hu, Y.; Cui, Z.; Zhou, J.; Wang, Y.; Zou, Z. Self-constructed facet junctions on hexagonal CdS single crystals with high photoactivity and photostability for water splitting. *Appl. Catal., B* **2019**, *244*, 694−703.
(22) Chen, F.; Huang, H.; Ye, L.; Zhang, T.; Zhang, Y.; Han, X.; Ma, T. Thickness-dependent facet junction control of layered $BiOIO_3$ single crystals for highly efficient CO_2 photoreduction. *Adv. Funct. Mater.* **2018**, *28*, 1804284.
(23) Tan, G.; Zhang, L.; Ren, H.; Wei, S.; Huang, J.; Xia, A. Effects of pH on the hierarchical structures and photocatalytic performance of $BiVO_4$ powders prepared via the microwave hydrothermal method. *ACS Appl. Mater. Interfaces* **2013**, *5*, 5186−5193.
(24) Thalluri, S. R. M.; Suarez, C. M.; Virga, A.; Russo, N.; Saracco, G. Insights from crystal size and band gap on the catalytic activity of monoclinic $BiVO_4$. *Int. J. Chem. Eng. Appl.* **2013**, *4*, 305.
(25) Wang, X.; Sø, L.; Su, R.; Wendt, S.; Hald, P.; Mamakhel, A.; Yang, C.; Huang, Y.; Iversen, B. B.; Besenbacher, F. The influence of crystallite size and crystallinity of anatase nanoparticles on the photodegradation of phenol. *J. Catal.* **2014**, *310*, 100−108.
(26) Yu, J.; Kudo, A. Effects of structural variation on the photocatalytic performance of hydrothermally synthesized $BiVO_4$. *Adv. Funct. Mater.* **2006**, *16*, 2163−2169.
(27) Chen, F.; Yang, Q.; Li, X.; Zeng, G.; Wang, D.; Niu, C.; Zhao, J.; An, H.; Xie, T.; Deng, Y. Hierarchical assembly of graphene-bridged Ag_3PO_4/Ag/$BiVO_4$ (040) Z-scheme photocatalyst: An efficient, sustainable and heterogeneous catalyst with enhanced visible-light photoactivity towards tetracycline degradation under visible light irradiation. *Appl. Catal., B* **2017**, *200*, 330−342.
(28) Obregón, S.; Caballero, A.; Colón, G. Hydrothermal synthesis of $BiVO_4$: Structural and morphological influence on the photocatalytic activity. *Appl. Catal., B* **2012**, *117*−*118*, 59−66.
(29) Li, H.; Sun, Y.; Cai, B.; Gan, S.; Han, D.; Niu, L.; Wu, T. Hierarchically Z-scheme photocatalyst of Ag@AgCl decorated on $BiVO_4$ (040) with enhancing photoelectrochemical and photocatalytic performance. *Appl. Catal., B* **2015**, *170*−*171*, 206−214.
(30) Li, J.; Zhou, J.; Hao, H.; Zhu, Z. Silver-modified specific (040) facet of $BiVO_4$ with enhanced photoelectrochemical performance. *Mater. Lett.* **2016**, *170*, 163−166.
(31) Tan, H. L.; Wen, X.; Amal, R.; Ng, Y. H. $BiVO_4$ {010} and {110} relative exposure extent: governing factor of surface charge population and photocatalytic activity. *J. Phys. Chem. Lett.* **2016**, *7*, 1400−1405.
(32) Li, R.; Zhang, F.; Wang, D.; Yang, J.; Li, M.; Zhu, J.; Zhou, X.; Han, H.; Li, C. Spatial separation of photogenerated electrons and holes among {010} and {110} crystal facets of $BiVO_4$. *Nat. Commun.* **2013**, *4*, 1432.
(33) Wang, D.; Jiang, H.; Zong, X.; Xu, Q.; Ma, Y.; Li, G.; Li, C. Crystal facet dependence of water oxidation on $BiVO_4$ sheets under visible light irradiation. *Chem. - Eur. J.* **2011**, *17*, 1275−1282.
(34) Wen, X. J.; Niu, C. G.; Guo, H.; Zhang, L.; Liang, C.; Zeng, G. M. Photocatalytic degradation of levofloxacin by ternary Ag_2CO_3/CeO_2/AgBr photocatalyst under visible-light irradiation: Degradation pathways, mineralization ability and an accelerated interfacial charge transfer process study. *J. Catal.* **2018**, *358*, 211−223.
(35) Kaur, A.; Kansal, S. K. Bi_2WO_6 nanocuboids: An efficient visible light active photocatalyst for the degradation of levofloxacin drug in aqueous phase. *Chem. Eng. J.* **2016**, *302*, 194−203.
(36) Kaur, A.; Salunke, D. B.; Umar, A.; Mehta, S. K.; Sinha, A. S. K.; Kansal, S. K. Visible light driven photocatalytic degradation of fluoroquinolone levofloxacin drug using Ag_2O/TiO_2 quantum dots: a mechanistic study and degradation pathway. *New J. Chem.* **2017**, *41*, 12079−12090.
(37) Yang, J.; Wang, D.; Zhou, X.; Li, C. A theoretical study on the mechanism of photocatalytic oxygen evolution on $BiVO_4$ in aqueous solution. *Chem. - Eur. J.* **2013**, *19*, 1320−1326.
(38) Tan, H. L.; Tahini, H. A.; Wen, X.; Wong, R. J.; Tan, X.; Iwase, A.; Kudo, A.; Amal, R.; Smith, S. C.; Ng, Y. H. Interfacing $BiVO_4$ with reduced graphene oxide for enhanced photoactivity: A tale of facet dependence of electron shuttling. *Small* **2016**, *12*, 5295−5302.
(39) Yu, J.; Low, J.; Xiao, W.; Zhou, P.; Jaroniec, M. Enhanced photocatalytic CO_2-reduction activity of anatase TiO_2 by co-exposed {001} and {101} facets. *J. Am. Chem. Soc.* **2014**, *136* (25), 8839−8842.
(40) Xiang, Q.; Jiaguo, Y.; Jaroniec, M. Tunable photocatalytic selectivity of TiO_2 films consisted of flower-like microspheres with exposed {001} facets. *Chem. Commun.* **2011**, *47*, 4532−4534.
(41) Yang, H. G.; Sun, C. H.; Qiao, S. Z.; Zou, J.; Liu, G.; Smith, S. C.; Cheng, H. M.; Lu, G. Q. Anatase TiO_2 single crystals with a large percentage of reactive facets. *Nature* **2008**, *453*, 638−641.
(42) Malathi, A.; Vasanthakumar, V.; Arunachalam, P.; Madhavan, J.; Ghanem, M. A. A low cost additive-free facile synthesis of $BiFeWO_6$/$BiVO_4$ nanocomposite with enhanced visible-light induced photocatalytic activity. *J. Colloid Interface Sci.* **2017**, *506*, 553−563.
(43) Gotić, M.; Musić, S.; Ivanda, M.; Šoufek, M.; Popović, S. Synthesis and characterisation of bismuth(III) vanadate. *J. Mol. Struct.* **2005**, *744*−*747*, 535−540.

https://dx.doi.org/10.1021/acs.inorgchem.0c01465
Inorg. Chem. 2020, 59, 10328−10342

(44) Sultana, S.; Mansingh, S.; Parida, K. M. Rational design of light induced self healed Fe based oxygen vacancy rich CeO_2 (CeO_2NS-FeOOH/Fe_2O_3) nanostructure materials for photocatalytic water oxidation and Cr(VI) reduction. *J. Mater. Chem. A* **2018**, *6*, 11377−11389.
(45) He, H.; Berglund, S. P.; Rettie, A. J. E.; Chemelewski, W. D.; Xiao, P.; Zhang, Y.; Mullins, C. B. Synthesis of $BiVO_4$ nanoflake array films for photoelectrochemical water oxidation. *J. Mater. Chem. A* **2014**, *2*, 9371−9379.
(46) Wang, S.; Chen, P.; Yun, J. H.; Hu, Y.; Wang, L. An electrochemically-treated $BiVO_4$ photoanode for efficient photoelectrochemical water splitting. *Angew. Chem., Int. Ed.* **2017**, *56*, 8500−8504.
(47) Nguyen Van, C.; Do, T. H.; Chen, J.-W.; Tzeng, W.-Y.; Tsai, K.-A.; Song, H.; Liu, H.-J.; Lin, Y.-C.; Chen, Y.-C.; Wu, C.-L.; Luo, C.-W.; Chou, W.-C.; Huang, R.; Hsu, Y.-J.; Chu, Y.-H. WO_3 mesocrystal-assisted photoelectrochemical activity of $BiVO_4$. *NPG Asia Mater.* **2017**, *9*, e357.
(48) Li, J.; Guo, L.; Lei, N.; Song, Q.; Liang, Z. Metallic Bi nanocrystals-modified defective $BiVO_4$ photoanodes exposed with (040) facets for photoelectrochemical water splitting. *ChemElectroChem* **2017**, *4*, 2852−2861.
(49) Guo, L.; Li, J.; Lei, N.; Song, Q.; Liang, Z. Morphological evolution and enhanced photoelectrochemical performance of V^{4+} self-doped, [010] oriented $BiVO_4$ for water splitting. *J. Alloys Compd.* **2019**, *771*, 914−923.
(50) Zhou, M.; Bao, J.; Xu, Y.; Zhang, J.; Xie, J.; Guan, M.; Wang, C.; Wen, L.; Lei, Y.; Xie, Y. Photoelectrodes based upon Mo:$BiVO_4$ inverse opals for photoelectrochemical water splitting. *ACS Nano* **2014**, *8*, 7088−7098.
(51) Kumar, S.; Ahirwar, S.; Satpati, A. K. Insight into the PEC and interfacial charge transfer kinetics at the Mo doped $BiVO_4$ photoanodes. *RSC Adv.* **2019**, *9*, 41368−41382.
(52) Li, C.; Zhu, X.; Zhang, H.; Zhu, Z.; Liu, B.; Cheng, C. 3D ZnO/Au/CdS sandwich structured inverse opal as photoelectrochemical anode with improved performance. *Adv. Mater. Interfaces* **2015**, *2*, 1500428.
(53) Yang, Y.; Zhong, X.; Liu, K.; Du, J.; Yang, Y.; He, H.; Zhou, Y.; Dong, F.; Fu, C.; Wang, J. Insight into the improvement mechanism of copper oxide/$BiVO_4$ heterojunction photoanodes for solar water oxidation. *J. Electrochem. Soc.* **2019**, *166*, H513−H520.
(54) Park, H. S.; Ha, H. W.; Ruoff, R. S.; Bard, A. J. On the improvement of photoelectrochemical performance and finite element analysis of reduced graphene oxide-$BiVO_4$ composite electrodes. *J. Electroanal. Chem.* **2014**, *716*, 8−15.
(55) Kim, C. W.; Son, Y. S.; Kang, M. J.; Kim, D. Y.; Kang, Y. S. (040)-Crystal facet engineering of $BiVO_4$ plate photoanodes for solar fuel production. *Adv. Energy Mater.* **2016**, *6*, 1501754.
(56) Nayak, S.; Swain, G.; Parida, K. M. Enhanced photocatalytic activities of RhB degradation and H_2 evolution from in situ formation of the electrostatic heterostructure MoS_2/NiFe LDH nanocomposite through the Z-scheme mechanism via p−n heterojunctions. *ACS Appl. Mater. Interfaces* **2019**, *11*, 20923−20942.
(57) Kandi, D.; Sahoo, D. P.; Martha, S.; Parida, K. M. Rational design of a coupled confronting Z-scheme system towards photocatalytic refractory pollutant degradation and water splitting reaction. *Adv. Mater. Interfaces* **2019**, *6*, 1900370.
(58) Paramanik, L.; Reddy, K. H.; Parida, K. M. An energy band compactable B-rGO/$PbTiO_3$ p−n junction: a highly dynamic and durable photocatalyst for enhanced photocatalytic H_2 evolution. *Nanoscale* **2019**, *11*, 22328−22342.
(59) Shan, L.; Lu, C.; Dong, L.; Suriyaprakash, J. Efficient facet regulation of $BiVO_4$ and its photocatalytic motivation. *J. Alloys Compd.* **2019**, *804*, 385−391.
(60) Karthikeyan, S.; Boopathy, R.; Sekaran, G. In situ generation of hydroxyl radical by cobalt oxide supported porous carbon enhance removal of refractory organics in tannery dyeing wastewater. *J. Colloid Interface Sci.* **2015**, *448*, 163−174.
(61) Kumar, A.; Rana, A.; Sharma, G.; Naushad, M.; Al-Muhtaseb, A. H.; Guo, C.; Juez, A. I.; Stadler, F. J. High performance photocatalytic hydrogen production and degradation of levofloxacin by wide spectrum responsive Ag/Fe_3O_4 bridged $SrTiO_3$/g-C_3N_4 plasmonic nano-junctions: Joint effect of Ag and Fe_3O_4. *ACS Appl. Mater. Interfaces* **2018**, *10*, 40474−40490.

https://dx.doi.org/10.1021/acs.inorgchem.0c01465
Inorg. Chem. 2020, 59, 10328−10342